

THE LENS REDSHIFT AND GROUP ENVIRONMENT FOR HE 0435-1223¹

N. D. MORGAN², C. S. KOCHANEK², O. PEVUNOVA³, P. L. SCHECHTER⁴

Draft version July 8, 2018

ABSTRACT

The redshift of the galaxy lensing HE 0435–1223 is 0.4546 ± 0.0002 , based on observations obtained with the Low Dispersion Survey Spectrograph 2 (LDSS2) on the Magellan Consortium’s 6.5 m Clay telescope. *Hubble Space Telescope*/ACS observations of the system also reveal a spiral-rich group of 10 galaxies within $40''$ of the elliptical lensing galaxy. The redshifts for two of these galaxies were measured to be in the foreground (at $z = 0.419$) with respect to the lens, thus at least some of the nearby galaxies are not part of the same physical group as the lensing galaxy. Mass models of the system (assuming same-plane deflectors) that take the local group environment into account do better at explaining the observed emission-line flux ratios (which are presumably unaffected by microlensing) than single halo models, but the match is still not perfect. In particular, component A (a minimum of the light travel time) is observed to be 0.20 mag brighter than predicted and component C (also a minimum image) is observed to be 0.16 mag fainter than predicted. Mass models for the system predict an A–D time delay of either 15.8 or 17.6 days ($H_o = 72 \text{ km s}^{-1} \text{ Mpc}^{-1}$) depending on the details of the local galaxy environment.

Subject headings: gravitational lensing: individual (HE 0435–1223)

1. INTRODUCTION

For a variety of reasons, follow-up observations of gravitationally lensed quasars have not kept pace with the lens discovery rate. For example, both lens and source redshifts are required to convert a measured time-delay into an estimate of the Hubble constant (Refsdal 1964) or to measure the mass-to-light evolution of lensing galaxies (Rusin et al. 2003), but only half of the ~ 80 known systems have complete redshift information. Poor knowledge of the lens galaxy environment also hinders lensing applications. Nearby groups or clusters can bias estimates of the Hubble constant by contributing some fraction of the lensing mass convergence (Gorenstein, Shapiro & Falco 1988; Saha 2000), and such structures are likely responsible for the large ($\sim 10\%$) shears required to model quadruple systems (Holder & Schechter 2003) and for explaining the observed quad-to-double ratio (Keeton & Zabludoff 2004). It is therefore important to understand the characteristics of each lens system as thoroughly as possible. In this paper, we report our measurement of the lens redshift for the quadruple quasar HE 0435–1223 and explore the system’s local galaxy environment from *HST*/ACS imaging.

HE 0435–1223 was discovered to be a $z = 1.689$ quasar during the Hamburg/ESO (HES) survey for bright quasars in the Southern Hemisphere

(Wisotzki et al. 2000). The quasar was later found to be gravitationally lensed by Wisotzki et al. (2002) during snapshot followups of HES quasars with the 6.5 m Baade telescope at the Las Campanas Observatory (LCO). The image morphology is a symmetric quad with image separations of $2''.3$ and $2''.6$ along the long axes of the configuration, somewhat reminiscent of the Northern Hemisphere “Einstein Cross” Q 2237+0305 (Huchra et al. 1985). The lensing galaxy was prominently detected in the Baade discovery images, with its light profile and *gri* aperture colors suggestive of a $0.3 < z < 0.5$ elliptical galaxy.

The system holds high promise for measuring a differential time delay and estimating the Hubble constant. Wisotzki et al. (2002) cite evidence for both short-term (20% over ~ 2 months) and long-term (1 magnitude over ~ 12 years) variability in the total quasar flux. The symmetric image configuration also implies relatively short differential time delays (on the order of several weeks), which ought to make it straightforward to distinguish the time-delay signature from longer-timescale microlensing variability.

Wisotzki et al. (2003) provided a refined galaxy redshift estimate of $z = 0.44 \pm 0.02$ based on integral field observations of the system. However, their estimate was obtained from low-resolution ($\Delta\lambda = 300\text{\AA}$) spectral rebinning that traced the galaxy’s overall spectral energy distribution rather than from the detection of stellar absorption features. In §2, we report a precise spectroscopic measurement of the lensing galaxy redshift of $z = 0.4546 \pm 0.0002$ using the Low-Dispersion Survey Spectrograph 2 (LDSS2) on the Clay 6.5 m telescope. In §3, we make use recent *HST*/ACS observations of the system to explore the HE 0435–1223 galaxy environment and find evidence for a spiral-rich group of at least 10 galaxies within $40''$, at least two of which are in the foreground (at $z = 0.419$) with respect to the lens. Overall the data suggest a complex lensing environment. We explore several lens models for the system using the

¹ Based on observations obtained with the Magellan Consortium’s Clay Telescope and the NASA/ESA *Hubble Space Telescope*. *HST* observations are obtained at the Space Telescope Science Institute, which is operated by the Association of Universities for Research in Astronomy, Inc., under NASA contract NAS 5-26555. These observations are associated with *HST* program 9744.

² Department of Astronomy, Ohio State University, Columbus, OH 43204; nmorgan@astronomy.ohio-state.edu, ckochanek@astronomy.ohio-state.edu

³ Infrared Processing and Analysis Center, M/S 100-22, California Institute of Technology, Jet Propulsion Laboratory, Pasadena, CA 91125; olga@ipac.caltech.edu

⁴ Department of Physics, Massachusetts Institute of Technology, Cambridge, MA 02139; schech@space.mit.edu

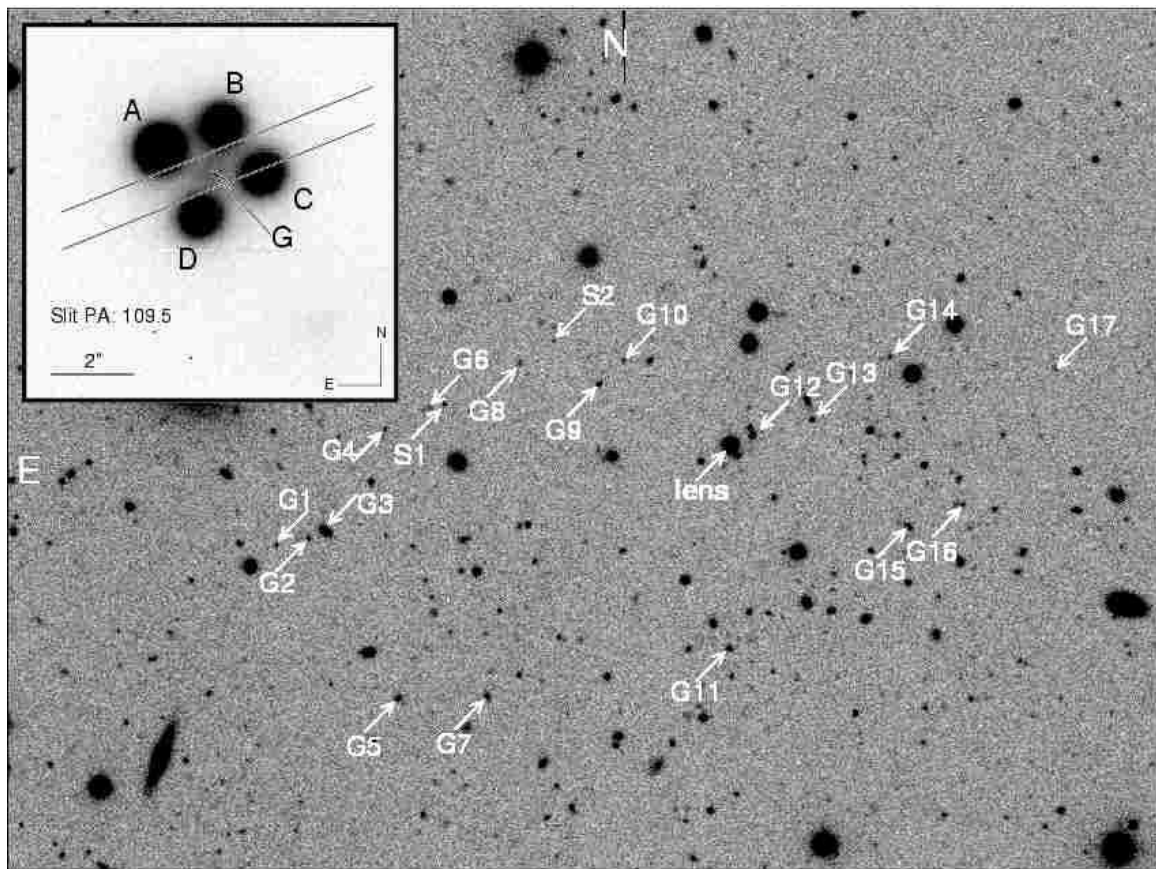


FIG. 1.— *R*-band image of HE0435–1223 and field obtained with the du Pont 2.5-m telescope at Las Campanas. The panel spans $7.1'$ across. Targets observed with LDSS-2 are labeled (S1, S2, lens, G1–17). *Inset*: Close-up of HE 0435–1223 from Figure 2 of Wisotzki et al. (2002). The parallel lines show the slit orientation and width used for LDSS2 spectroscopy.

HST/ACS astrometry and emission-line flux ratios from Wisotzki et al. (2003) in §4, and discuss the model implications and time-delay predictions in §5.

2. MAGELLAN/LDSS2 OBSERVATIONS

HE 0435–1223 was observed on 2002 December 11 using the Low Dispersion Survey Spectrograph 2 (LDSS2; Allington-Smith et al. 1994) at the Magellan Consortium’s Clay telescope at LCO. The LDSS2 is a multi-slit spectrograph with a $7'$ diameter field of view and $0''.378$ pixel^{-1} CCD detector. We used the medium-red grism blazed at 6000 \AA , which provided a nominal dispersion of $5.3 \text{ \AA pixel}^{-1}$ and a useful wavelength coverage of 4500 \AA to 8500 \AA . A slit width of $0''.74$ was used for all targets when constructing the aperture mask. The night was photometric and the Shack-Hartmann wavefront sensor helped to deliver an image quality of $\sim 0''.5$ FWHM.

In addition to the lensing galaxy, we obtained simultaneous spectra of 19 objects within $3'$ of HE 0435–1223 (see Figure 1). Our observing sequence consisted of two 30 minute exposures with slits centered on the lensing galaxy and surrounding field galaxies, followed by two 10 minute exposures through the same mask but offset by $1''.25$ to the North-East. These last two observations were used to obtain quasar template spectra of components A and B (Figure 1 inset), which were subsequently used to remove quasar spillover from the lens galaxy spectrum. No spectrophotometric standards were observed.

Initial data reduction consisted of bias-subtraction, flat-fielding, and removing cosmic-rays by interpolating from neighboring pixels. The two-dimensional spectra were then averaged together to produce a single on-galaxy and off-galaxy image.

Since these are two-dimensional spectra, care must be taken when deriving a wavelength solution and performing the extraction. The wavelength calibration was obtained using night sky lines bracketing each target spectrum. We identified eight lines from the spectral atlas of Osterbrock et al. (1996), providing roughly uniform coverage between $[\text{O I}]\lambda 5577$ and $\text{OH}\lambda 8827$. The lines were identified on 2–4 dispersion rows (depending on the target slit length) with two rows always straddling the target spectrum, providing 16–32 points of known wavelength as a function of CCD row and column. We then fit a fourth order polynomial along the dispersion direction and a linear fit along the spatial direction, which provided the wavelength solution as a function of pixel position on the chip. The wavelength solution with respect to the reference lines was extremely good: rms better than 0.8 \AA (0.15 pixels) for all spectra. The sky background was then removed by fitting and subtracting a line to the sky level for each CCD column.

The spectral dispersion was mostly parallel to the CCD rows, but did bend by several pixels in the vertical from blue to red. To define the extraction path for the lensing galaxy, we fit two overlapping Gaussian profiles to each

TABLE 1
 REDSHIFT ANALYSIS FOR HE 0435-1223 LENS AND FIELD GALAXIES

Object	R.A.	Dec.	z	Line Identification
G1 ...	4 38 26.03	-12 18 4.6	0.8124 ± 0.0001	[O II]/H β /[O III]
G2 ...	4 38 25.25	-12 18 1.2	0.3183 ± 0.0003	[O II]/H β /[O III]
G3 ...	4 38 24.85	-12 17 58.1	0.3021 ± 0.0002	[O II]/[O III]/H α
G4 ...	4 38 23.54	-12 17 19.0	0.3915 ± 0.0005	[O II]/H β /[O III]
G5 ...	4 38 22.69	-12 18 57.4	0.6240 ± 0.0007	[O II]/[O III]
G6 ...	4 38 22.48	-12 17 9.9	0.6676 ± 0.0004	[O II]/[O III]
G7 ...	4 38 20.46	-12 18 54.1	0.5580 ± 0.0001	[O II]/H β
G8 ...	4 38 20.32	-12 16 50.7	0.1841 ± 0.0002	H β /[O III]
G9 ...	4 38 18.28	-12 16 56.2	0.3380	[O II]?
G10 ..	4 38 17.73	-12 16 46.9	0.3691	[O II]?
G11 ..	4 38 14.50	-12 18 29.2	0.4579 ± 0.0001	[O II]/H β /[O III]
G12 ..	4 38 24.85	-12 17 58.1	0.4191 ± 0.0002	[O II]/H β /[O III]
G13 ..	4 38 12.88	-12 17 2.6	0.4189	[O II]?
G14 ..	4 38 11.06	-12 16 37.7	0.4872 ± 0.0005	[O II]/CaII H&K
G15 ..	4 38 10.26	-12 17 39.4	0.3766 ± 0.0001	[O II]/[O III]
G16 ..	4 38 8.93	-12 17 29.9	0.6880 ± 0.0001	CaII H&K
G17 ..	4 38 6.90	-12 16 37.5	0.8434	[O II]?
lens ..	4 38 14.87	-12 17 14.8	0.4546 ± 0.0002	CaII H&K
S1	4 38 22.13	-12 17 8.3	0	Star
S2	4 38 19.52	-12 16 41.6	0	Star

NOTE. — Redshifts for galaxies observed with LDSS2. IDs correspond to labels in Figure 1. Redshift errors are the rms dispersion among multiple lines (when available), and do not include the $\delta z = 0.0002$ uncertainty in the underlying wavelength calibration. All positions are J2000.0 coordinates.

CCD column to model the flux from the A+B spectra. A second-order polynomial fit to A’s center as a function of chip column gave a good fit to the dispersion drift (fit rms of 0.08 pixels), and was subsequently used as the extraction path for both the quasar and lensing galaxy

spectra. The extraction was performed using a three pixel ($1''.1$) width for quasar components A and B, and a two pixel ($0''.76$) width for the lensing galaxy. For the remaining targets, we used a wide extraction width of 6 pixels ($2''.3$) parallel to the CCD rows.

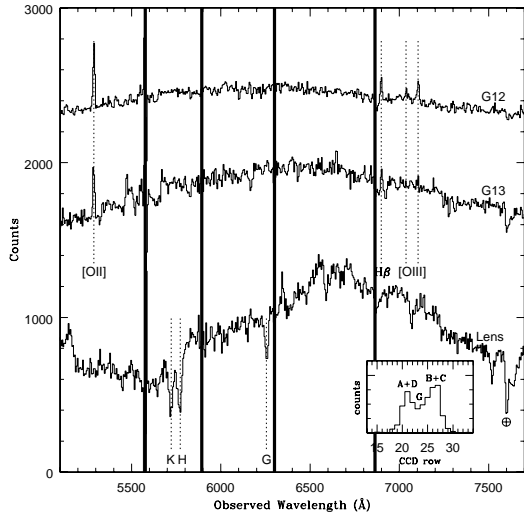


FIG. 2.— Spectra of the lensing galaxy (bottom) and neighboring galaxies G12 and G13 (top and middle). The lens spectrum is shown after subtracting 0.2 times component A’s spectrum. The four vertical strips denote skylines used for wavelength calibration. The lens, G13, and G12 spectra have been shifted by 100, 1500, and 2250 counts, respectively, for clarity. *Inset*: Slice along the spatial direction for the lens galaxy spectrum. The two peaks correspond to spillover flux from the A+D and B+C quasar images, with the lens galaxy in the middle.

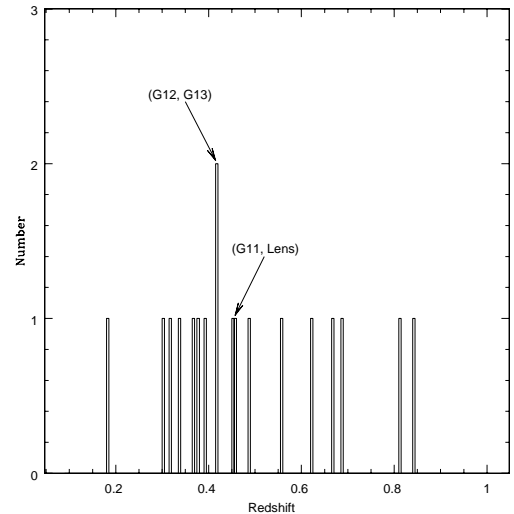


FIG. 3.— Redshift histogram of galaxies observed with the LDSS2.

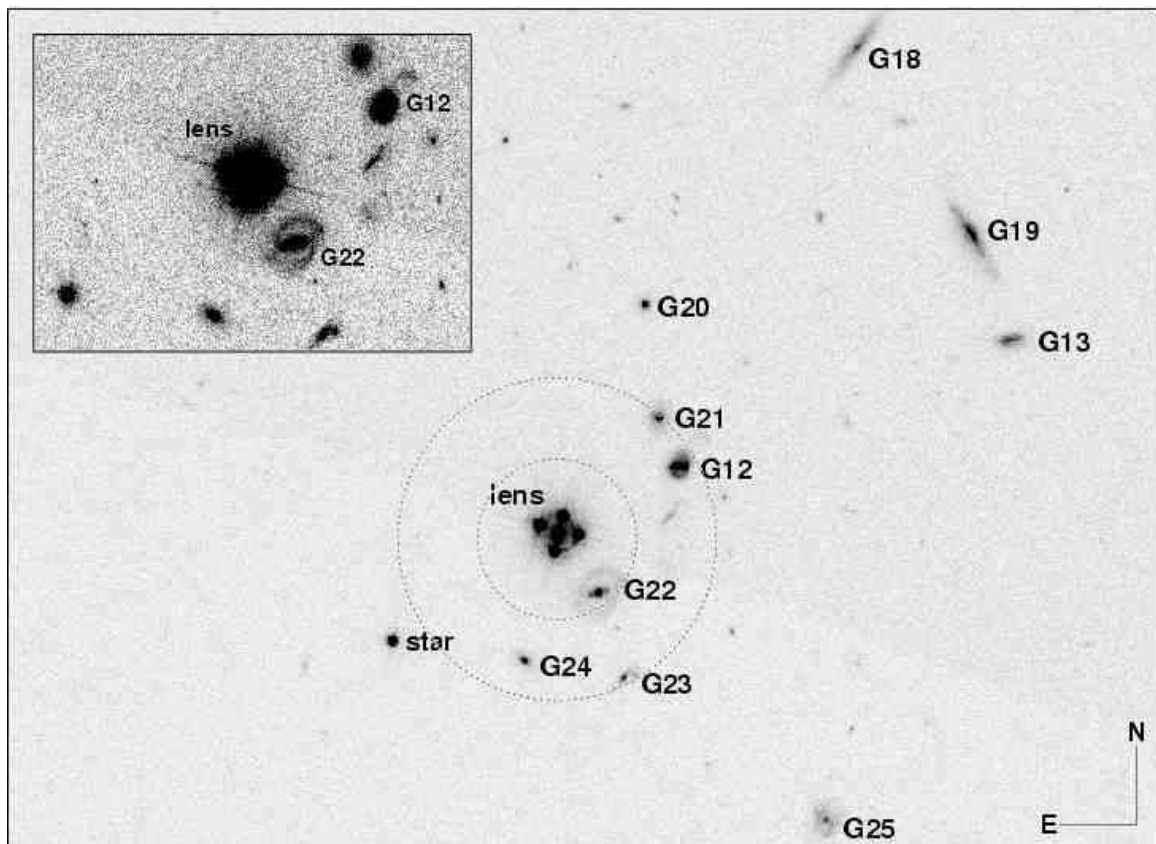


FIG. 4.— PyDrizzled *HST*/ACS F814W image of HE 0435–1223 and field. Prominent nearby galaxies are labeled. The concentric circles centered on the lensing galaxy mark 5'' and 10'' radii. Inset shows the inner 10'' region (centered on the lens) at high contrast.

Figure 2 shows the extracted lens galaxy spectrum after subtracting 0.2 times component A’s spectrum, with the scale factor chosen such that the blueward side of the Mg II broad emission line at $\sim 7500 \text{ \AA}$ appeared smoothly subtracted by eye. The Ca II H&K absorption features are visible, as well as the 4000 \AA break and G band absorption line. Fortunately, the Ca II H&K feature fell 150 \AA redward of the [O I] $\lambda 5777$ skyline, which provided points for wavelength calibration on either side of the feature.

To determine the galaxy redshift, we simultaneously fit for the the continuum plus two overlapping Gaussian profiles to the Ca II H&K absorption feature and bracketing continuum using an appropriately fixed rest-wavelength separation. This does a good job of modeling the absorption feature (reduced chi-squared of 0.7) and yields a best-fit redshift of $z = 0.4546$. The uncertainty in the fit is of the same order as the error in the wavelength calibration, $\sim 1 \text{ \AA}$, translating to a redshift uncertainty of 0.0002.

Figure 2 also shows the extracted spectra for galaxies G12 and G13, the two closest galaxies from the lens that we obtained spectra for ($\Delta\theta=8''.9$ and $\Delta\theta=31''.4$ from the lens, respectively). Both show [O II] $\lambda 3727$ emission at $\sim 5300 \text{ \AA}$, and G12 also shows weak H β and [O III] $\lambda\lambda 4959, 5007$ emission lines at $\sim 7000 \text{ \AA}$. Gaussian fits to the emission lines give redshifts of $z = 0.4191 \pm 0.0002$ and $z = 0.4189$ for G12 and G13, respectively.

Table 1 lists the spectroscopic redshifts obtained for all

18 galaxies observed with LDSS2, and Figure 3 shows the redshift histogram. There is no obvious group or cluster along the line of sight from the limited redshift sample, although the coincident G12,G13 redshifts at $z = 0.419$ suggests some overdensity at that redshift. The redshift difference between the G12,G13 pair and the lensing galaxy is $7,500 \text{ km s}^{-1}$ in the G12,G13 restframe, an order of magnitude larger than expected for cluster association and even more so for a group, so the galaxies are not physically associated. The closest galaxy in redshift space to the lens is G11 ($z = 0.4579$) at a projected separation of $\Delta\theta=74''.6$ (proper distance of 420 kpc), which is too far to significantly affect the lensing potential.

3. *HST*/ACS OBSERVATIONS

HE 0435–1223 was observed with the Advanced Camera for Surveys/Wide Field Camera (ACS/WFC; Ford et al. 1998) onboard the *Hubble Space Telescope* on 2003 August 18 as part of the CASTLES imaging program of gravitationally lensed quasars (principal investigator, C. Kochanek; PID 9744). Five images each through the F555W and F814W filters were obtained (hereafter *V* and *I*) with respective total integration times of approximately 34 and 24 minutes. The data were reduced using the IRAF/CALACS⁵ package as part of the “on-the-fly” reprocessing at the time of download. Subsequent

⁵ IRAF is distributed by the National Optical Astronomy Observatories, which are operated by the Association of Universities for Research in Astronomy, Inc., under cooperative agreement with the National Science Foundation.

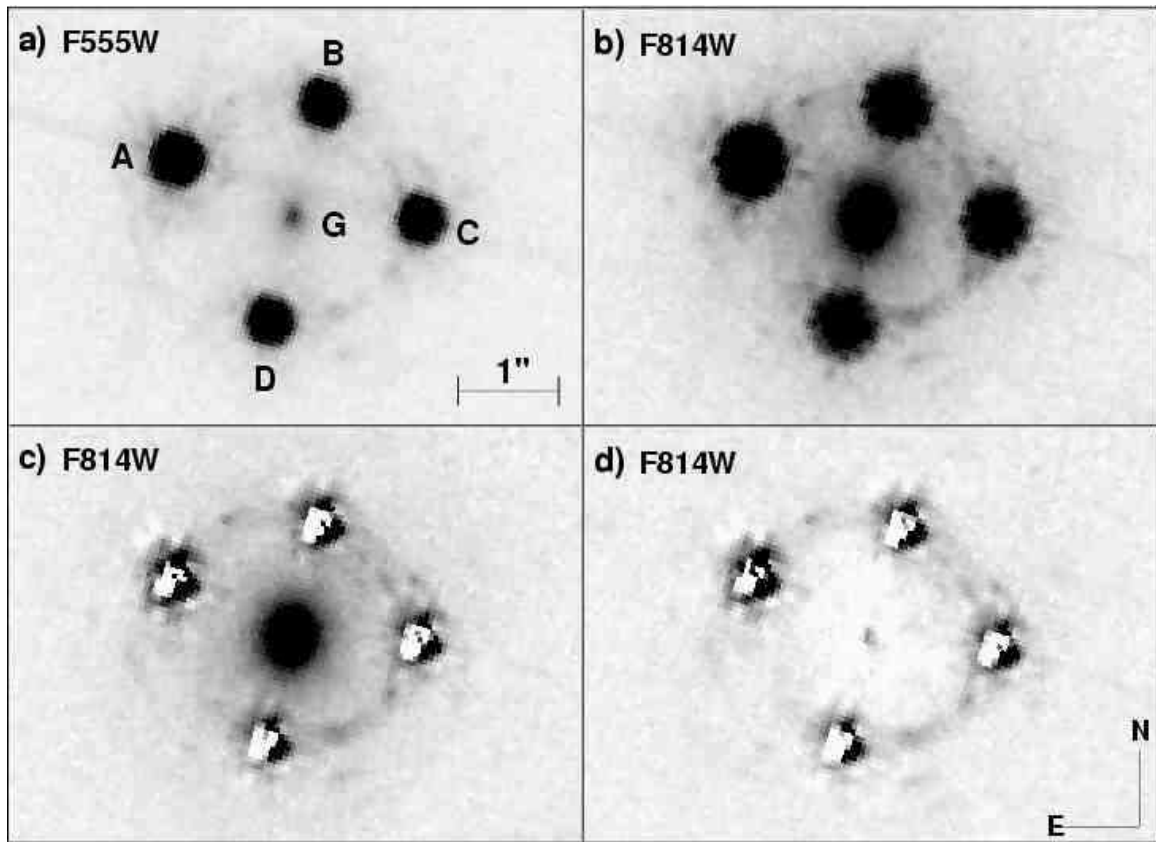


FIG. 5.— (a): PyDrizzled *HST*/F555W observations of HE 0435–1223. (b): PyDrizzled *HST*/F814W observations of HE 0435–1223. (c): Same as (b), but after subtracting the best four-component PSF model. (d): Same as (b), but after subtracting the best four-component PSF plus de Vaucouleurs model for the lensing galaxy. Contrast in all panels is from $-0.02 e^-s^{-1}$ to $0.5 e^-s^{-1}$.

cosmic-ray rejection, geometric correction, and image combinations were performed using the standard PyRAF programs available for ACS data reduction.

Figure 4 shows the geometrically-corrected *I*-band image after combining with PyDrizzle. The environment around the lens appears to contain a spiral-rich group of galaxies. There are 5 prominent galaxies within $10''$ (outer dashed circle), the closest of which (G22) is within $5''$ and corresponds to the SW companion galaxy originally noted by Wisotzki et al. (2002). Its image morphology is a barred spiral with arms that appear to thread back onto the central bulge. Galaxies G12 and G13 from §2 are also labeled. Both show a bulge+disk image morphology, face-on in the case of G12 and edge-on in the case of G13, with several bright knots visible distinct from the central nucleus in both galaxies. The image morphologies are consistent with ongoing star formation as implied by the $[O II]\lambda 3727 \text{ \AA}$ emission-lines observed in the respective spectra. Galaxies G18, G19, G23, and G25 also suggest either face-on or edge-on spirals, while G20, G21, and G24 appear to be ellipticals.

The *V*- and *I*-band closeup images of HE 0435–1223 are shown in Figure 5a and 5b. The image configuration is consistent with previous ground-based images of the system, although the *HST* data do reveal multiple partial arcs tracing the system’s Einstein radius in both the *V*- and *I*-band images. One can also see lensed knots at two different radii embedded in the arc emission and which likely arises from lensed structure of the quasar

host galaxy. To obtain the relative image positions, we modeled the light distribution using PSFs generated with the TinyTim v6.1a software of Krist & Hook (2003) and a circularly symmetric de Vaucouleurs profile (with effective radius of $1''2$; see below) convolved with the *HST* PSF for the lensing galaxy. The PSFs were generated taking into account the lens position on the WFC and mapped onto a 4×4 oversampled grid to assist with sub-pixel shifts. The relative positions and fluxes of the five-component model were then simultaneously solved for using a Powell (Press et al. 1992) minimization routine. The solutions were obtained in the two filters using both the individual (geometrically distorted) ‘fit’ images and the undistorted drizzled frames, and we found that the relative quasar positions agreed to within $0''.002$ using the different datasets. The galaxy center rms was $0''.005$ ($0''.002$) along the cardinal directions for the *V*(*I*)-band solutions, roughly an order of magnitude improvement over the earlier position obtained from ground-based observations.

The averaged relative offsets obtained from the ‘fit’ *I*-band solutions are reported in Table 2. To our initial surprise, the relative quasar positions differed by up to 6σ when compared to the Magellan offsets given by Wisotzki et al. (2002), even though both datasets quote similar astrometric precision. The differences, however, could be described by a 0.6% scale discrepancy between the two datasets, in the sense that the Wisotzki et al. (2002) measurements correspond to a larger angular size than

TABLE 2
HST/ACS ASTROMETRY AND PHOTOMETRY FOR HE 0435–1223

Object	Δ R.A. (")	Δ Dec. (")	V/V_A	I/I_A	V-band	I-band
A.....	$\equiv 0$	$\equiv 0$	$\equiv 1$	$\equiv 1$	18.545 ± 0.001	19.106 ± 0.001
B.....	-1.4772 ± 0.002	$+0.5532 \pm 0.002$	0.607 ± 0.016	0.621 ± 0.003	19.082 ± 0.001	19.623 ± 0.001
C.....	-2.4687 ± 0.002	-0.6033 ± 0.002	0.579 ± 0.012	0.617 ± 0.003	19.149 ± 0.001	19.631 ± 0.001
D.....	-0.9377 ± 0.002	-1.6147 ± 0.002	0.557 ± 0.010	0.516 ± 0.003	19.196 ± 0.001	19.824 ± 0.001
G.....	-1.1687 ± 0.002	-0.5723 ± 0.002	20.80 ± 0.10	19.83 ± 0.08

NOTE. — Relative image positions and system flux ratios are from PSF fitting as described in the text. Quasar apparent magnitudes are from $0''.5$ aperture photometry plus a nominal 0.1 mag aperture correction. Galaxy magnitudes have been obtained using the best-fit *I*-band de Vaucouleurs profile, with error bars corresponding to 10% uncertainties in r_e . All magnitudes have been placed onto the STMAG system.

the *HST*/ACS measurements. After correcting for the scale difference, the Magellan and *HST* astrometry agree to better than 1σ .

The reconstructed *I*-band image without the four quasars (Figure 5c) allows us to investigate the detailed morphological properties of the lensing galaxy. We modeled the galaxy’s *I*-band light distribution of the PSF-subtracted image using GALFIT (Peng et al. 2002), taking care to mask the ring of pixels tracing the quasar residuals and arc emission during the fit. The best-fit elliptical $r^{1/4}$ law gave an axis ratio of 0.83, a position angle of -7.4° East of North, and an effective radius r_e of $1''.20$ (6.6 kpc at the lens redshift). Figure 5d shows the residuals after subtracting the best-fit profile.

The effective surface brightness of the galaxy μ_e , defined as the average flux inside the effective radius, is 22.22 mag in *I*-band. To get a handle on the *V*-band effective surface brightness, we applied the same *I*-band effective radius and normalized the de Vaucouleurs profile using the PSF-subtracted *V*-band image. This gave $\mu_e = 23.19$ mag in *V*-band. The total lens galaxy magnitude in the two filters then follows from $m_{tot} = \mu_e - 5.0 \log r_e - 2.5 \log 2\pi$ and are reported in Table 2.

In Table 3, we list apparent magnitudes and relative positions for the 10 prominent galaxies labeled in Figure 4 and for three nearby reference stars. Galaxy aperture magnitudes were computed using a $2''.0$ radius with error bars estimated from the Poisson noise inside each aperture. Stellar magnitudes were computed using a $0''.5$ aperture radius and a nominal 0.1 mag aperture correction.

4. LENS MODELS AND TIME DELAY PREDICTIONS

Predicting differential time delays between the quasar images requires an accurate mass model of the lensing galaxy and its environment. Wisotzki et al. (2002) found that a simple singular isothermal sphere (SIS) embedded in an external shear did a good job at modeling the quasar positions (rms of 1.3 mas), but failed to account for the quasar flux ratios. When compared to their *i*-band fluxes, the SIS+shear model (which only used position constraints) underpredicted component A’s flux by 0.35 mag. Overall, it predicted components B+C to be almost a full magnitude (0.86 mag) brighter relative to components A+D than observed.

Such discrepancies are common when modeling strong lenses, and it is generally accepted that the image fluxes are perturbed either by substructure along the line of

sight (Dalal & Kochanek 2002) or by microlensing from stars in the lensing galaxy (Schechter & Wambsgans 2002). These two processes are in principle distinguishable from each other since they yield different predictions for extended sources. The flux ratios ought not to show a strong dependence on source size if significant substructure is present, but will show a source size effect for microlensing-induced perturbations. This is because larger source sizes will average over small-scale structure present in the microlensing caustic pattern, driving the system flux ratios toward the macromodel values. In practice, since the quasar broad-line region is several orders of magnitude larger than the continuum emitting region, then the emission-line fluxes ought to be much less sensitive to microlensing than the broad-band fluxes.

The C IV and C III] emission-line fluxes for HE 0435–1223 were measured by Wisotzki et al. (2003) using the Potsdam Multi-Aperture Spectrophotometer (PMAS) on the Calar-Alto 3.5 m telescope. They indeed found that the emission-line flux ratios were in better agreement with model predictions than were the broad-band values, but the match was still far from acceptable: component A was underpredicted by 0.26 mag and the combined B+C flux was still 0.57 mag brighter with respect to components A+D than observed. Attempts to force the SIS+shear model to reproduce the emission-line flux ratios could be achieved only with significant ($\sim 50\sigma$) deviations between the observed and model image positions. This difficulty could be a consequence of the simple isothermal model used for the lensing potential and a more realistic model, perhaps taking the group environment into account, might be more successful.

In this section, we explore several mass models for the system in an effort to reproduce the *HST*/ACS astrometry and the Wisotzki et al. (2003) emission-line photometry. Our basic mass model is a singular isothermal ellipsoid (SIE; Kassiola & Kovner (1993), Kormann et al. (1994)) with convergence κ given by

$$\kappa = \frac{\Sigma}{\Sigma_c} = \frac{b}{2r} \left(\frac{1}{1 + \epsilon \cos 2(\theta - \theta_e)} \right)^{1/2}, \quad (1)$$

where Σ is the projected surface mass density, $\Sigma_c = (c^2/2\pi G)(D_d/D_l D_{ls})$ is the critical surface mass density, ϵ is the ellipticity parameter related to the axis ratio q by $q^2 = (1 - \epsilon)/(1 + \epsilon)$, and the major axis is orientated along θ_e . The mass parameter b is given by

$$b = 4\pi \left(\frac{\sigma}{c} \right)^2 \frac{D_{ls}}{D_s}, \quad (2)$$

TABLE 3
HST/ACS ASTROMETRY AND PHOTOMETRY FOR HE 0435–1223 FIELD

Object	Δ R.A. (")	Δ Dec. (")	V-band	I-band
G12 ..	−8.96	3.66	21.182 ± 0.018	21.158 ± 0.009
G13 ..	−30.18	11.42	22.486 ± 0.047	21.980 ± 0.015
G18 ..	−20.37	29.56	22.147 ± 0.043	21.829 ± 0.012
G19 ..	−27.69	18.01	21.517 ± 0.019	21.230 ± 0.009
G20 ..	−6.74	13.64	23.946 ± 0.155	22.776 ± 0.033
G21 ..	−7.62	6.61	22.564 ± 0.056	21.819 ± 0.013
G22 ..	−3.75	−4.21	22.253 ± 0.042	21.260 ± 0.010
G23 ..	−5.39	−9.46	24.409 ± 0.204	22.850 ± 0.035
G24 ..	1.01	−8.39	23.946 ± 0.155	22.501 ± 0.024
G25 ..	−18.36	−18.25	22.134 ± 0.025	21.910 ± 0.014
S1....	9.48	−7.16	21.415 ± 0.004	20.258 ± 0.002
S2....	11.59	−51.29	20.183 ± 0.002	19.250 ± 0.001
S3....	−41.98	67.73	20.152 ± 0.002	20.575 ± 0.002

NOTE. — Galaxy magnitudes were obtained using a 2''0 aperture radius, with error bars corresponding to Poisson noise inside the aperture. Stellar magnitudes are from 0''5 aperture photometry plus a nominal 0.1 mag aperture correction. All magnitudes have been placed onto the STMAG system.

where σ is the line-of-sight velocity dispersion of the dark matter halo. Distances D_l , D_s , and D_{ls} are angular diameter distances to the lens, the source, and from the lens to source, respectively. For the SIS model ($q = 1$), b is also the system's Einstein radius. The two-dimensional effective lensing potential ϕ can then be found from $\nabla^2\phi = 2\kappa$, and is simply $\phi = br$ for the spherically symmetric case (e.g., Narayan & Bartelmann 1999). We also consider environmental effects by adding a shear term ϕ_γ of the form

$$\phi_\gamma = -\gamma \frac{r^2}{2} \cos 2(\theta - \theta_\gamma), \quad (3)$$

where γ is the shear strength and the sign convention is for θ_γ to point toward (or away) from the mass responsible for the shear.

We consider three models, defined as follows:

$$\phi_{ISx} = \phi_{SIS} + \phi_\gamma \quad (4)$$

$$\phi_{IEx} = \phi_{SIE} + \phi_\gamma \quad (5)$$

$$\phi_{IEISx} = \phi_{SIE} + \phi_{SIS,G22} + \phi_\gamma. \quad (6)$$

Model ISx is a singular isothermal sphere for the lensing galaxy plus external shear. It is the same model used by Wisotzki et al. (2002). Model IEx adds a second shear axis by using an elliptical isothermal halo plus external shear. Model IEISx explicitly takes the galaxy environment into account. It adds a third shear axis by fixing a second isothermal halo at the position of the closest neighboring galaxy G22.

For constraints, we use the *HST*/ACS positions listed in Table 2 with 2 mas error circles for the quasar positions and a 5 mas error circle for the galaxy position. The lens galaxy position is allowed to vary, but its position is constrained using the above error circle. The averaged C IV and C III] emission-line fluxes can be computed from Table 2 of Wisotzki et al. (2003) and give B/A, C/A, and D/A ratios of 0.76, 0.71, and 0.54, respectively. Wisotzki et al. (2003) quote formal errors for the emission-line fluxes on the order of 1%. While we consider models with 1% flux errors, we also consider models with 10% flux

errors to account for unmodeled effects such as intrinsic quasar variability. We also assume identical redshifts for all deflectors, even though the LDSS2 spectroscopy from §2 has already showed that this is not strictly the case ($\Delta z = 0.036$ for the lensing galaxy and G12,G13). Throughout this section, we adopt an $(\Omega_m, \Omega_\Lambda) = (0.3, 0.7)$ cosmology, set the Hubble constant to $72 \text{ km s}^{-1} \text{ Mpc}^{-1}$, and quote all angular positions as degrees East of North. All models are minimized in the image-plane using the *gravlens* software of Keeton et al. (2001). Model results are summarized in Table 4.

4.1. Single Halo: Models ISx and IEx

Wisotzki et al. (2003) found that an isothermal halo plus external shear cannot simultaneously fit the Magellanic positions and emission-line flux ratios. We find a similar result using the *HST*/ACS positions as constraints. Using 10% flux errors, the ISx model does well to reproduce the image positions ($\theta_{rms} = 2.7$ mas), but predicts components B+C to be 0.59 mag brighter with respect to components A+D than observed. In particular, component A's model flux is 0.28 mag fainter than observed. This is essentially the same result found by Wisotzki et al. (2003) using just the Magellanic image positions as constraints. Tightening the flux errors to 1% does not yield an improvement: θ_{rms} worsens to 5.4 mas and the image magnifications are mostly unchanged (see Table 4).

The IEx model allows for two shear axes, external shear plus galaxy ellipticity. One has to be careful when solving for the shear and ellipticity terms since an approximate degeneracy exists between the two effects (Keeton et al. 1997). To sift through the degeneracy, we solved for (b, γ, e) over a grid of initial conditions for $(\theta_\gamma, \theta_e)$ and focused on the region of parameter space that gave the lowest χ^2 values. The best-fit model using 10% flux errors fit the quasar positions essentially exactly ($\theta_{rms} = 0.2$ mas), but again had trouble predicting the flux ratios, with the combined B+C flux 0.61 mag brighter with respect to A+D than observed. The problem again is chiefly component A, which is predicted to be 0.25 too faint.

TABLE 4
LENS MODEL RESULTS FOR HE 0435–1223

Parameter	ISx		IEx		IEISx	
	10%	1%	10%	1%	10%	1%
$\chi^2/\text{dof} \dots\dots$	21.3/6	816/6	9.7/4	134/4	5.8/3	87.3/3
$\chi_{pos}^2 \dots\dots\dots$	7.1	28.9	0.0	32.3	0.0	13.3
$\chi_{flux}^2 \dots\dots\dots$	8.3	775	8.6	43.3	5.5	15.9
$\chi_{gal}^2 \dots\dots\dots$	5.9	11.3	1.1	59.0	0.2	58.4
θ_{rms} (mas) ..	2.7	5.4	0.2	5.7	0.2	3.7
Δm_A (mag)	0.28	0.28	0.25	0.05	0.20	0.03
Δm_B (mag)	-0.10	-0.09	-0.07	-0.04	0.01	-0.01
Δm_C (mag)	-0.13	-0.13	-0.16	-0.03	-0.16	0.00
Δm_D (mag)	0.08	0.07	0.12	0.03	0.05	-0.02
b (arcsec) ..	1.20	1.20	1.20	1.17	1.17	1.17
b' (arcsec)	0.18	0.30
$\gamma \dots\dots\dots$	0.08	0.08	0.01	0.14	0.04	0.14
$e \dots\dots\dots$	0.13	0.30	0.22	0.29
$\theta_\gamma \dots\dots\dots$	-13.8	-13.8	-15.9	-30.0	-28.0	-27.3
$\theta_e \dots\dots\dots$	-11.5	60.0	-14.1	60.2
τ_{B-A} (days)	5.48	5.40	7.18	1.88	8.72	1.87
τ_{C-A} (days)	0.61	0.44	0.85	-0.14	0.70	-0.18
τ_{D-A} (days)	12.21	11.89	15.80	4.25	17.54	4.07

NOTE. — Model results for the isothermal sphere plus external shear (ISx), isothermal ellipsoid plus external shear (IEx), and isothermal ellipsoid plus external shear and isothermal sphere centered on G22 (IEISx). Models are minimized using 10% and 1% emission-line flux errors. θ_{rms} gives the rms between predicted and observed quasar images. Mass parameters b and b' are for the lens and G22 galaxies, respectively. Magnitude differences are in the sense predicted minus observed.

The galaxy parameters do agree with the observed characteristics: the model ellipticity e (defined as 1 minus the axis ratio) was 0.13 and pointed along $-11^\circ.5$, which is close to the measured values of 0.17 and $-7^\circ.4$ for the light distribution.

Tightening the IEx flux errors to 1% improved the flux predictions — within 0.05 mag for all four components — but the galaxy parameters became unreasonable: the ellipticity was 0.29, almost twice as large than observed, and pointed nearly perpendicular ($\Delta\theta = 70^\circ$) from the observed orientation. Moreover, the galaxy position shifted by $0''.038$ (7-8 σ) from its measured center. Overall the model can be rejected since it predicts halo properties in strong disagreement with the observed galaxy properties. Thus neither of the single halo models are consistent with both the observed galaxy properties and the system’s emission-line flux ratios.

4.2. Multiple Halos: Model IEISx

The shear direction for the ISx and IEx models pointed roughly at -15° . Naively one would expect it to point toward the closest neighboring galaxy G22 at 216° (or equivalently 36°). The same difference was found Wisotzki et al. (2002) and led them to speculate that the neighboring galaxy might simply be a chance projection. Another possibility is that G22 does have a significant effect on the lensing potential, but that a second perturber NW of the lens dominates the shear contribution. Figure 4 shows that this is plausible. Galaxies G12,

G20, and G21 (as well as G18, G19 and G13 farther out) range from position angles of -20° to -70° and their aggregate mass or associated halo may dominate the shear measurement.

Model IEISx takes both shear directions into account by using a halo centered on G22 for the SW perturber plus an external shear for the NW perturber. Using 10% flux errors, the model does just as well as the IEx model in predicting the image positions ($\theta_{rms} = 0.2$ mas) and also slightly improves the flux predictions. This time the B+C flux was only 0.40 mag brighter with respect to A+D than observed, component A was too faint by 0.20 mag, and component C was too bright by 0.16 mag. The galaxy ellipticity was also slightly larger than observed, 0.22 compared to 0.17, but did point within 7° of the measured orientation. The shear strength for the 10% model was 0.04 and pointed at -28° , or about 13° closer to the G20-G21-G12 group than found in the single halo IEx model. We again reject the 1% model since it gives unreasonable galaxy parameters (see Table 4) despite the improved image fluxes.

5. DISCUSSION

The improved flux predictions and closer alignment between the shear direction and the NW group are arguments for favoring the multiple halo model, but the shear still does not point to any obvious perturber. It points between the faint G20 and G21 galaxies as seen from the lens. This is about $+20^\circ$ from the G20-G21-G12 flux-weighted center and about $+30^\circ$ from G12, the brightest

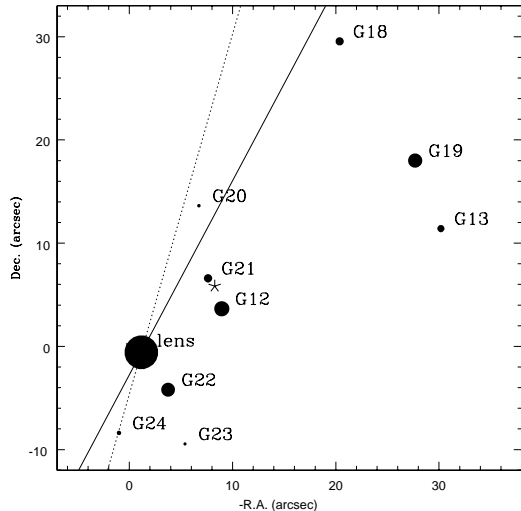


FIG. 6.— Diagram showing relative galaxy positions (filled circles). Dot sizes are proportional to the respective galaxy’s I -band flux within a $2''$ aperture. The diagonal lines show the shear directions for the IEx (dotted) and IEISx (solid) lens models. The star marks the flux-weighted center of the G20-G21-G12 group of galaxies.

of all neighboring galaxies within $40''$ of the lens (see Figure 6). We know that G12 is at essentially the same redshift as the lensing galaxy, so if the only significant perturbers were G12 to the NW and G22 to the SW, then we would expect the IEISx shear to point directly toward G12. It does not, which suggests that if the flux ratios are to be explained solely by the macromodel, then the lensing potential must be even more complicated than the double halo model considered here.

Alternatively, the macromodel could be essentially correct and a separate effect could be perturbing the flux ratios. In general, there are four mechanisms that could alter the image fluxes: microlensing, quasar variability, differential dust extinction and substructure lensing. Presumably microlensing is not an issue since we are working with the emission-line fluxes. Quasar variability is also not a factor since the A–C time delay is less than a day in all models, much too short compared to quasar variability timescales (typically weeks to months).

Wisotzki et al. (2002) already commented that extinction is probably not very important for this system since the lensing galaxy is an elliptical and the Magellanic colors of the four quasars agreed to $\lesssim 0.05$ mag. In general, Falco et al. (1999) found median differential extinctions among a subsample of optically-selected lenses of $\Delta E(B - V) = 0.04$ mag. Only 10% of their sightlines through elliptical galaxies have $0.15 < \Delta E(B - V) < 0.25$, so the ~ 0.2 mag of extinction needed to reconcile component C’s relative faintness is unlikely but not impossible. However, the PMAS resolved spectral observations of the four quasars obtained by Wisotzki et al. (2003) show the quasar continuum slopes to be virtually identical (L. Wisotzki, private communication). This would be a strong coincidence if any significant dust extinction were present, and of course rules out significant differential extinction.

The remaining explanation is substructure lensing.

Millilensing by low-mass satellites (typically modeled as NFW profiles or truncated isothermal halos) in the lens galaxy can either brighten or dim image fluxes by several tenths of a magnitude. The effect has been modeled both for individual systems (Metcalf & Zhao 2002) and in a statistical sense (Dalal & Kochanek 2002), and typically requires the subclumps to comprise a few percent by mass of the primary galaxy’s dark-matter halo. Although we do not consider substructure models here, such an effect remains the most plausible explanation of the HE 0435–1223 emission-line fluxes given the present data.

We do note that substructure lensing by strictly isothermal halos, either embedded in the lensing galaxy or along the line of sight, cannot account for the observed flux ratios. Isothermal mass clumps always brighten positive-parity images (Keeton 2003), but components A and C, both positive-parity images, are respectively brighter and fainter than predicted. Of course the unlensed quasar flux is a free parameter, so one could dim the source such that both A and C became brighter than predicted, but then images B and D (both negative-parity images) would be ~ 0.2 mag brighter than predicted as well. Millilensing (and microlensing as well) tends to dim saddle-point images (Keeton 2003, Schechter & Wambsganss 2002), so the situation using isothermal halos becomes somewhat contrived.

We can predict the differential time delays for the system using the measured lens redshift of $z = 0.4546 \pm 0.0002$ from §2. The A–D delay is the longest delay and therefore the most interesting to measure. The ISx, IEx, and IEISx models predict A–D delays of 12.21, 15.80, and 17.54 days, respectively. The elliptical halo (IEx) is formally preferred over the spherical halo (ISx) with χ^2/dof of 3.6 compared to 2.4, where the improvement comes wholly from the quasar and galaxy positions. The double halo (IEISx) is preferred over the single halo (IEx) with χ^2/dof of 2.4 compared to 1.9, where the improvement comes mostly from the images fluxes. The last two models yield 10% differences in the A–D time delay, which gives an estimate of the error that one can expect from uncertainties in the local galaxy environment.

There are several ways to improve the time delay prediction. Redshift information for the remaining 8 of 10 neighboring galaxies, especially for G22, would significantly improve the model confidence. In the least, it would point to which galaxies might share a common dark matter halo and thus guide the choice of parametric models. The *HST*/ACS images already show a partial Einstein ring for the system in I -band, and one would suspect a complete Einstein ring to be visible in the infrared. The extra constraints offered by modeling the ring may be able to distinguish between the single and double halo models without recourse to the image flux ratios. For example, it would be interesting to see if the shear direction for a ring-constrained IEISx model points more in line with the center of the NW group than found here.

This work is based on observations made with the NASA/ESA *Hubble Space Telescope*, obtained at the Space Telescope Science Institute, which is operated by AURA, Inc., under NASA contract NAS5-26555. This

research is supported by HST grants G0-9375 and GO-9744. PLS acknowledges support from the US NSF under

AST02-06010.

REFERENCES

- Allington-Smith, J., Breare, M., Ellis, R., Gellatly, D., Glazebrook, K., Jordan, P., Maclean, J., Oates, P., Shaw, G., Tanvir, N., Taylor, K., Taylor, P., Webster, J., Worswick, S. 1994, *PASP*, 106, 983
- Dalal, N. & Kochanek, C. S. 2002, *ApJ*, 572, 25
- Falco, E. E., Impey, C. D., Kochanek, C. S., Lehár, J., McLeod, B. A., Rix, H.-W., Keeton, C. R., Muñoz, J. A. & Peng, C. Y. 1999, *ApJ*, 523, 617
- Ford, H. C., Bartko, F., Bely, P. Y., Broadhurst, T., Burrows, C. J., Cheng, E. S., Clampin, M., Crocker, J. H., Feldman, P. D., Golimowski, D. A., Hartig, G. F., Illingworth, G., Kimble, R. A., Lesser, M. P., Miley, G., Neff, S. G., Postman, M., Sparks, W. B., Tsvetanov, Z., White, R. L., Sullivan, P., Krebs, C. A., Leviton, D. B., La Jeunesse, T., Burmester, W., Fike, S., Johnson, R., Slusher, R. B., Volmer, P., Woodruff, R. A. 1998, *Proc. SPIE*, 3356, 234-248
- Gorenstein, M. V., Shapiro, I. I. & Falco, E. E. 1988, *ApJ*, 327, 693
- Holder, G. & Schechter, P. L. 2003, *ApJ*, 2003, 688
- Huchra, J., Gorenstein, M., Kent, S., Shapiro, I., Smith, G., Horine, E., Perley, R. 1985, *AJ*, 90, 691
- Kassiola, A. & Kovner, I. 1993, *ApJ*, 417, 450
- Keeton, C. R., Kochanek, C. S. & Seljak, U. 1997, *ApJ*, 482, 604
- Keeton, C. R. 2001 (*astro-ph 0102340*)
- Keeton, C. R. 2003, *ApJ*, 584, 664
- Keeton, C. R. & Zabludoff, A. I. 2004, *ApJ*, 612, 660
- Kormann, R., Schneider, P. & Bartelmann, M. 1994, *A&A*, 284, 285
- Krist, J. E. & Hook, R. N. 2003, *The Tiny Time User's Guide*, Version 6.1a (Baltimore: STScI)
- Metcalf, R. B. & Zhao, H. 2002, *ApJ*, 567, L5
- Narayan, R. & Bartelmann, M. 1999, in *Formation of Structure in the Universe*, ed. A. Dekel & J. Ostriker (Cambridge: Cambridge Univ. Press)
- Osterbrock, D. E., Fulbright, J. P., Martel, A. R., Keane, M. J., Trager, S. C., Basri, G. 1996, *PASP*, 108, 277
- Peng, C. Y., Ho, L. C., Impey, C. D. & Rix, H.-W. 2002, *AJ*, 124, 266
- Press, W. H., Teukolsky, S. A., Vetterling, W. T. & Flannery, B. P. 1992, *Numerical Recipes in C* (Cambridge: Cambridge Univ. Press)
- Refsdal, S. 1964, *MNRAS*, 128, 307
- Rusin, D., Kochanek, C. S., Falco, E. E., Keeton, C. R., McLeod, B. A., Impey, C. D., Lehár, J., Muñoz, J. A., Peng, C. Y., Rix, H.-W. 2003, *ApJ*, 587, 143
- Saha, P. 2000, *AJ*, 120, 1654
- Schechter, P. L. & Wambsganss, J. 2002, *ApJ*, 580, 685
- Wisotzki, L., Christlieb, N., Bade, N., Beckmann, V., Köhler, T., Vanelle, C., Reimers, D. 2000, *A&A*, 358, 77
- Wisotzki, L., Schechter, P. L., Bradt, H. V., Heinmüller, J., Reimers, D. 2002, *A&A*, 395, 17
- Wisotzki, L., Becker, T., Christensen, L., Helms, A., Jahnke, K., Kelz, A., Roth, M. M., Sanchez, S. F. 2003, *A&A*, 408, 455